ICES REPORT 11-12

May 2011

Discretization of higher-order gradient damage models using isogeometric finite elements

by

Clemens V. Verhoosel, Michael A. Scott, Michael J. Borden, Thomas J.R. Hughes, and René de Borst

Report Documentation Page		*Form Approved* *OMB No. 0704-0188*

Public reporting burden for the collection of information is estimated to average 1 hour per response, including the time for reviewing instructions, searching existing data sources, gathering and maintaining the data needed, and completing and reviewing the collection of information. Send comments regarding this burden estimate or any other aspect of this collection of information, including suggestions for reducing this burden, to Washington Headquarters Services, Directorate for Information Operations and Reports, 1215 Jefferson Davis Highway, Suite 1204, Arlington VA 22202-4302. Respondents should be aware that notwithstanding any other provision of law, no person shall be subject to a penalty for failing to comply with a collection of information if it does not display a currently valid OMB control number.

1. REPORT DATE **MAY 2011**	2. REPORT TYPE	3. DATES COVERED **00-00-2011 to 00-00-2011**
4. TITLE AND SUBTITLE **Discretization of higher-order gradient damage models using isogeometric finite elements**		5a. CONTRACT NUMBER
		5b. GRANT NUMBER
		5c. PROGRAM ELEMENT NUMBER
6. AUTHOR(S)		5d. PROJECT NUMBER
		5e. TASK NUMBER
		5f. WORK UNIT NUMBER
7. PERFORMING ORGANIZATION NAME(S) AND ADDRESS(ES) **University of Texas at Austin,Institute for Computational Engineering and Sciences,Austin,TX,78712**		8. PERFORMING ORGANIZATION REPORT NUMBER
9. SPONSORING/MONITORING AGENCY NAME(S) AND ADDRESS(ES)		10. SPONSOR/MONITOR'S ACRONYM(S)
		11. SPONSOR/MONITOR'S REPORT NUMBER(S)

12. DISTRIBUTION/AVAILABILITY STATEMENT
Approved for public release; distribution unlimited

13. SUPPLEMENTARY NOTES

14. ABSTRACT
Continuum damage formulations are commonly used for the simula- tion of diffuse fracture processes. Implicit gradient damage models are employed to avoid the spurious mesh dependencies associated with lo- cal continuum damage models. The C0-continuity of traditional finite elements has hindered the study of higher-order gradient damage approx- imations. In this contribution we use isogeometric finite elements, which allow for the construction of higher-order continuous basis functions on complex domains. We study the suitability of isogeometric finite elements for the discretization of higher-order gradient damage approximations.

15. SUBJECT TERMS

16. SECURITY CLASSIFICATION OF:			17. LIMITATION OF ABSTRACT	18. NUMBER OF PAGES	19a. NAME OF RESPONSIBLE PERSON
a. REPORT **unclassified**	b. ABSTRACT **unclassified**	c. THIS PAGE **unclassified**	**Same as Report (SAR)**	**24**	

Standard Form 298 (Rev. 8-98)
Prescribed by ANSI Std Z39-18

Discretization of higher-order gradient damage models using isogeometric finite elements

Clemens V. Verhoosel[1,2], Michael A. Scott[2], Michael J. Borden[2],
Thomas J.R. Hughes[2], and René de Borst[1]

[1] *Eindhoven University of Technology, Department of Mechanical Engineering,
Eindhoven, The Netherlands*
[2] *The University of Texas at Austin, Institute for Computational Engineering and
Sciences, Austin, USA*

Abstract

Continuum damage formulations are commonly used for the simulation of diffuse fracture processes. Implicit gradient damage models are employed to avoid the spurious mesh dependencies associated with local continuum damage models. The C^0-continuity of traditional finite elements has hindered the study of higher-order gradient damage approximations. In this contribution we use isogeometric finite elements, which allow for the construction of higher-order continuous basis functions on complex domains. We study the suitability of isogeometric finite elements for the discretization of higher-order gradient damage approximations.

1 INTRODUCTION

Continuum damage models [1] are widely used for the simulation of diffuse fracture processes. Several modifications of the original theory have been proposed to overcome the mesh dependency problems associated with the absence of an internal length scale (see e.g. [2, 3]). One way to avoid mesh dependencies is to relate the material parameters to the element size [4, 5]. Alternatively, an internal length scale can be introduced by a spatial smoothing function in the continuum formulation [6]. Gradient approximations of this smoothing function have led to the development of damage models where an internal length scale is introduced through gradients of an equivalent strain field. Among the gradient damage formulations, the implicit gradient enhancement [7] is considered the most effective. In its original form a second-order Taylor expansion is used to approximate a smoothing integral, which results in a system of two second-order partial differential equations. This formulation is attractive from a discretization point of view since it can be solved using C^0-continuous finite elements. It has, however, been demonstrated that the accuracy of the second-order approximation can be limited [8, 9]. For that reason it is important to study the

effect of the higher-order terms in the Taylor approximation of the nonlocal formulation, which result in higher-order gradient damage formulations.

Mixed finite element formulations can be used for the discretization of higher-order gradient damage formulations. In these formulations, the introduction of higher-order continuous basis functions is avoided by introducing auxiliary fields. This results in systems with many more degrees of freedom than required by the second-order gradient formulation, making the method computationally expensive. To avoid the introduction of auxiliary fields, meshless methods have been used [9]. The smoothness of meshless methods is inherently derived from the way in which the basis functions are constructed. Although meshless methods have been applied successfully for the discretization of the fourth-order gradient damage formulation, they have not been used widely. A reason for this is the inability of meshless methods to define geometry [10]. The incompatibility with traditional finite element formulations, in the sense that the method is not element-based, may be another reason why meshless methods are not commonly applied to higher-order gradient damage formulations.

In this contribution we use isogeometric finite elements to overcome the problems associated with the use of mixed formulations and meshless methods for gradient damage formulations. The isogeometric analysis concept was introduced by Hughes et al. [11] and has been applied successfully to a wide variety of problems in solids, fluids and fluid-structure interactions (see [12] for an overview). Use of higher-order, smooth spline bases in isogeometric analysis has computational advantages over standard finite elements, especially when higher-order differential equations are considered [13]. In contrast to meshless methods, the geometry and solution space are one and the same. This makes it possible to construct bases for complex geometries, which can be obtained directly from a computer aided design (CAD) tool [14]. From an analysis point of view isogeometric analysis can be considered as an element-based discretization technique. This compatibility with traditional finite elements facilitates the application to industrial problems.

We first review the nonlocal continuum damage formulation and the gradient-based approximation in section 2. We then introduce in section 3 the isogeometric finite element discretization. In section 4 we present numerical simulations utilizing isogeometric finite elements for the discretization of the second-order, fourth-order and sixth-order gradient formulations.

2   ISOTROPIC DAMAGE FORMULATION

We consider a body $\Omega \subset \mathbb{R}^N$ with $N \in \{1, 2, 3\}$ and boundary $\partial\Omega$ (see Figure 1). The displacement of a material point $x \in \Omega$ is denoted by $u(x) \in \mathbb{R}^N$. The displacements satisfy Dirichlet boundary conditions, $u_i = \tilde{u}_i$, on $\partial\Omega_{u_i} \subseteq \partial\Omega$. Under the assumption of small displacement gradients, the infinitesimal strain tensor

$$\varepsilon_{ij} = u_{(i,j)} = \frac{1}{2}\left(\frac{\partial u_i}{\partial x_j} + \frac{\partial u_j}{\partial x_i}\right) \tag{1}$$

2
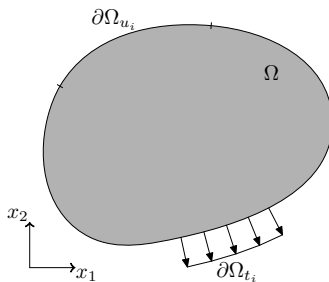
Figure 1: Solid domain Ω with boundary $\partial\Omega$.

is used as an appropriate measure for the deformation of the body. The Cauchy stress tensor, $\sigma(x) \in \mathbb{R}^{N \times N}$, is used as the corresponding stress measure. An external traction $\tilde{t}_i$ acts on the Neumann boundary $\partial\Omega_{t_i} \subseteq \partial\Omega$ and is equal to the projection of the stress tensor on the outward pointing normal vector $n(x) \in \mathbb{R}^N$, i.e. $\tilde{t}_i = \sigma_{ij} n_j$. The solid body is loaded by increasing the boundary tractions or boundary displacements.

2.1 Constitutive modeling

In isotropic continuum damage models, the Cauchy stress is related to the infinitesimal strain tensor by

$$\sigma_{ij} = (1 - \omega) H_{ijkl} \varepsilon_{kl}, \tag{2}$$

where $\omega \in [0, 1]$ is a scalar damage parameter and H is the Hookean elasticity tensor for undamage material (i.e. with $\omega = 0$). When damage has fully developed ($\omega = 1$) a material has lost all stiffness. Note that we adopt index notation with summation from 1 to N over repeated italic subscript indices, for example, $u_i v_i = \sum_{i=1}^{N} u_i v_i$.

The damage parameter is related to a history parameter κ by a monotonically increasing function $\omega = \omega(\kappa)$, which is referred to as the damage law. Various damage laws will be considered in the numerical simulations section. The history parameter evolves according to the Kuhn-Tucker conditions

$$f \leq 0, \quad \dot{\kappa} \geq 0, \quad \dot{\kappa} f = 0 \tag{3}$$

for the loading function $f = \bar{\eta} - \kappa$, where $\bar{\eta}$ is a nonlocal strain measure, referred to as the nonlocal equivalent strain. The monotonicity of both κ and $\omega(\kappa)$ guarantees that the damage parameter is monotonically increasing at every material point, thereby introducing irreversibility in the constitutive model.

Nonlocality is introduced into the model by means of the nonlocal equivalent strain which ensures a well-posed formulation at the onset of damage evolution. If instead the damage parameter was related to a local strain measure, η, the resulting medium would suffer from a local loss of ellipticity in the case of material softening [15]. The model is then unable to smear out the damage

3

zone over a finite volume. In other words, a local continuum damage formulation fails to introduce a length scale for the damage zone, resulting in spurious mesh dependencies in numerical solutions.

A straightforward way of introducing nonlocality in the formulation is by defining the nonlocal equivalent strain, $\bar{\eta}(x)$, as the volume average of a local equivalent strain, $\eta = \eta(\varepsilon)$,

$$\bar{\eta}(x) = \frac{\int\limits_{y \in \Omega} g(x,y)\eta(y)\,\mathrm{d}y}{\int\limits_{y \in \Omega} g(x,y)\,\mathrm{d}y}, \tag{4}$$

where $g(x,y)$ is the weighting function

$$g(x,y) = \exp\left(-\frac{\|x-y\|^2}{2l_c^2}\right). \tag{5}$$

We refer to this model as the nonlocal damage formulation [6]. The local equivalent strain maps the strain tensor onto a scalar.

Although the nonlocal formulation is straightforward, it requires the computation of a volume integral for the evaluation of the constitutive behavior at every material point. This makes the numerical implementation both cumbersome and inefficient. In particular, the stiffness matrix is full. Even when truncated, the nonlocal operator has a negative impact on the sparsity of the matrix. This results in computationally expensive assembly and solution routines. To circumvent these deficiencies, approximations of the integral equation are commonly used.

The nonlocal equivalent strain (4) can be approximated by substitution of a Taylor expansion for the equivalent strain field around the point x

$$\eta(y) = \eta|_{y=x} + \frac{\partial\eta}{\partial y_i}\bigg|_{y=x}(y_i - x_i) + \frac{1}{2}\frac{\partial\eta}{\partial y_i \partial y_j}\bigg|_{y=x}(y_i - x_i)(y_j - x_j) + \mathcal{O}((x_i - y_i)^3). \tag{6}$$

Assuming the solid volume stretches to infinity leads to the gradient approximation of equation (4)

$$\bar{\eta}(x) = \eta(x) + \frac{1}{2}l_c^2\frac{\partial^2\eta}{\partial x_i^2}(x) + \frac{1}{8}l_c^4\frac{\partial^4\eta}{\partial x_i^2\partial x_j^2}(x) + \frac{1}{48}l_c^6\frac{\partial^6\eta}{\partial x_i^2\partial x_j^2\partial x_k^2}(x) + \ldots \tag{7}$$

This gradient approximation is known as the explicit gradient formulation. As an alternative, the implicit gradient formulation (e.g. Ref. [7]) is obtained by direct manipulation of equation (7)

$$\bar{\eta}(x) - \frac{1}{2}l_c^2\frac{\partial^2\bar{\eta}}{\partial x_i^2}(x) + \frac{1}{8}l_c^4\frac{\partial^4\bar{\eta}}{\partial x_i^2\partial x_j^2}(x) - \frac{1}{48}l_c^6\frac{\partial^6\bar{\eta}}{\partial x_i^2\partial x_j^2\partial x_k^2}(x) + \ldots = \eta(x). \tag{8}$$

Because only C^0-continuity is required for the second-order approximation, the corresponding implicit gradient formulation has enjoyed widespread use.

In the remainder of this work we study the convergence of the implicit gradient formulation toward the nonlocal formulation upon increasing the number of gradient terms involved. If we truncate equation (8) after the d-th derivative, we can rewrite it using a linear operator $\mathcal{L}^d$ as

$$\mathcal{L}^d \bar{\eta}(x) = \eta(x). \tag{9}$$

We restrict ourselves to the second-order ($d = 2$), fourth-order ($d = 4$) and sixth-order ($d = 6$) implicit gradient damage formulations.

2.2 Implicit gradient damage formulation

In contrast to the nonlocal and explicit gradient damage formulations, the implicit formulation requires the solution of a boundary value problem for the nonlocal equivalent strain field, $\bar{\eta}(x)$, in addition to the usual problem for the displacement field, $u(x)$. In the absence of body forces, the resulting boundary value problem for the d-th order formulation is given by

$$\begin{cases} \frac{\partial \sigma_{ij}}{\partial x_j} = 0 & \forall x \in \Omega \\ \mathcal{L}^d \bar{\eta} = \eta \\ \sigma_{ij} n_j = \tilde{t}_i & \forall x \in \partial\Omega_{t_i} \\ \frac{\partial}{\partial x_n}\left(\frac{\partial^\alpha \bar{\eta}}{\partial x_j \dots}\right) = 0 & \forall x \in \partial\Omega, \, \alpha \in \{0, \dots, d-2\} \\ u_i = \tilde{u}_i & \forall x \in \partial\Omega_{u_i} \end{cases} \tag{10}$$

where $\tilde{t}$ and $\tilde{u}$ are the prescribed boundary traction and displacements, respectively. Notice that we assume all directional derivatives, $\frac{\partial}{\partial x_n} = n_i \frac{\partial}{\partial x_i}$, of the nonlocal equivalent strain field are zero on the boundary. We verify this choice numerically by comparing the results with the nonlocal formulation based on the integral equation (4). The kinematic and constitutive relations (1) and (2) are used to express the Cauchy stress in terms of the displacement field.

We solve the system (10) using the Galerkin method. The same solution spaces are used for the displacement field and nonlocal equivalent strain field, denoted by $\mathcal{S}_i^u \subset H^{\frac{d}{2}}(\Omega)$ and $\mathcal{S}^{\bar{\eta}} \subset H^{\frac{d}{2}}(\Omega)$, respectively. We denote our trial spaces as $\mathcal{V}_i^u$ and $\mathcal{V}^{\bar{\eta}}$ and assume that $\mathcal{V}^{\bar{\eta}} = \mathcal{S}^{\bar{\eta}}$ and $\mathcal{V}_i^u$ and $\mathcal{S}_i^u$ are the same modulo inhomogeneous boundary conditions. The weak form of equation (10) then follows as

$$\begin{cases} \left(\sigma_{ij}, v_{(i,j)}^u\right)_\Omega = \left(\tilde{t}_i, v_i^u\right)_{\partial\Omega} & \forall v_i^u \in \mathcal{V}_i^u \\ \left(\bar{\eta} - \eta, v^{\bar{\eta}}\right)_\Omega + \sum_{\beta=1}^{d/2}\left(\mathcal{H}^\beta \bar{\eta}, \mathcal{H}^\beta v^{\bar{\eta}}\right)_\Omega = 0 & \forall v^{\bar{\eta}} \in \mathcal{V}^{\bar{\eta}} \end{cases} \tag{11}$$

where $v_{(i,j)}^u = \frac{1}{2}\left(\frac{\partial v_i^u}{\partial x_j} + \frac{\partial v_j^u}{\partial x_i}\right)$ and $(\cdot, \cdot)_\Omega$ is the L^2-inner product. No boundary terms appear in the equation for the equivalent strain field, since the derivatives of this field in the direction of the normal vector are assumed zero on the

boundary of the domain. For the damage formulations considered in this work (i.e., with $d \in \{2, 4, 6\}$), the linear operator $\mathcal{H}^\beta$ is written as

$$\mathcal{H}^1 = \frac{l_c}{\sqrt{2}} \frac{\partial}{\partial x_i}, \quad \mathcal{H}^2 = \frac{l_c^2}{\sqrt{8}} \frac{\partial^2}{\partial x_i \partial x_j}, \quad \mathcal{H}^3 = \frac{l_c^3}{\sqrt{48}} \frac{\partial^3}{\partial x_i \partial x_j \partial x_k}. \qquad (12)$$

3 ISOGEOMETRIC FINITE ELEMENTS

Discretization of the weak formulation (11) for the d-th order damage formulation requires $(\frac{d}{2} - 1)$-times continuously differentiable basis functions. With isogeometric finite elements C^{p-1}-continuous basis functions can be constructed using splines of order p. We will consider B-splines and non-uniform rational B-splines (NURBS) [16]. Although T-splines [17] are considered beyond the scope of this contribution, it is emphasized that a unified analysis approach for splines is provided by Bézier extraction [18].

3.1 Univariate B-splines and NURBS

The fundamental building block of isogeometric analysis is the univariate B-spline, e.g. [16, 12]. A univariate B-spline is a piecewise polynomial defined over a knot vector $\Xi = \{\xi_1, \xi_2, \dots, \xi_{n+p+1}\}$, with n and p denoting the number and order of basis functions, respectively. The knot values ξ_i are non-decreasing with increasing knot index i, i.e. $\xi_1 \leq \xi_2 \leq \dots \leq \xi_{n+p+1}$. A partition of the parameter space $[\xi_1, \xi_{n+p+1})$ is provided by the elements

$$\Xi_e = \left[\xi_{\imath(e)}, \xi_{\imath(e)+1} \right) \qquad (13)$$

where $\imath(e)$ is a map from the element indices to the knot vector indices.

The B-spline basis is defined recursively, starting with the zeroth order ($p = 0$) functions

$$N_{i,0}(\xi) = \begin{cases} 1 & \xi_i \leq \xi < \xi_{i+1} \\ 0 & \text{otherwise} \end{cases} \qquad (14)$$

from which the higher-order ($p = 1, 2, \dots$) basis functions can be constructed using the Cox-de Boor recursion formula [19, 20]

$$N_{i,p}(\xi) = \frac{\xi - \xi_i}{\xi_{i+p} - \xi_i} N_{i,p-1}(\xi) + \frac{\xi_{i+p+1} - \xi}{\xi_{i+p+1} - \xi_{i+1}} N_{i+1,p-1}(\xi). \qquad (15)$$

Efficient and robust algorithms exist for the evaluation of these non-negative basis functions and their derivatives, e.g. [21]. B-spline basis functions satisfy the partition of unity property and B-spline parameterizations possess the variation diminishing property, e.g. [22]. An example of a univariate B-spline basis is shown in Figure 2. For notational convenience, we will drop the subscript p of the basis functions.

A B-spline is defined as a linear combination of B-spline basis functions

$$a(\xi) = \sum_{i=1}^{n} N_i(\xi) A_i, \tag{16}$$

where A_i is called a control point or variable. Equation (16) is typically used for the parameterization of curves in two (with $X_i \in \mathbb{R}^2$) or three (with $X_i \in \mathbb{R}^3$) dimensions by

$$x(\xi) = \sum_{i=1}^{n} N_i(\xi) X_i. \tag{17}$$

In combination with equation (13), this parametric map provides a definition of the elements in the physical space

$$\Omega_e = \{x(\xi), \ \xi \in \Xi_e\}. \tag{18}$$

B-splines used for analysis purposes are generally open B-splines, i.e., the first and last knot values have a multiplicity of $p+1$. Dirichlet boundary conditions can be applied to the control points on the boundary of the domain in the same way as done for the nodal variables in traditional finite elements. B-splines can also be refined, which is important in the context of isogeometric analysis, e.g. [23].

A drawback of B-splines is their inability to exactly represent many objects of engineering interest, such as conic sections. For this reason NURBS, which are a rational generalization of B-splines, are commonly used. A NURBS is defined as

$$a(\xi) = \sum_{i=1}^{n} R_i(\xi) A_i, \tag{19}$$

with the NURBS basis functions defined as

$$R_\beta(\xi) = \frac{N_\beta(\xi) W_\beta}{w(\xi)}, \tag{20}$$

where $w(\xi) = \sum_{i=1}^{n} N_i(\xi) W_i$ is called the weighting function. Note that in equation (20) no summation is performed over the repeated index β. In the special case that $W_i = c \ \forall i \in \{1, \ldots, n\}$, and c an arbitrary constant, the NURBS basis reduces to the B-spline basis.

3.2 Multivariate B-splines and NURBS

Computational domains in two and three dimensions can be parametrized by means of bivariate and trivariate splines, respectively. An N-variate B-spline is contructed over the tensor product of knot vectors

$$\Xi = \Xi^1 \otimes \ldots \otimes \Xi^N = \left\{\xi_1^1, \ldots, \xi_{n_1+p_1+1}^1\right\} \otimes \ldots \otimes \left\{\xi_1^N, \ldots, \xi_{n_N+p_N+1}^N\right\}. \tag{21}$$
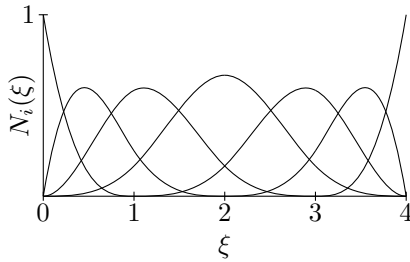
Figure 2: Third order B-spline basis for the global knot vector $\Xi = \{0, 0, 0, 0, 1, 2, 3, 4, 4, 4, 4\}$.

where n_α and p_α are the number of basis functions and order of the basis functions in the direction α, respectively. The parameter space $[\xi_1^1, \xi_{n_1+p_1+1}^1) \otimes \ldots \otimes [\xi_1^N, \xi_{n_N+p_N+1}^N)$ is partitioned by the elements

$$\Xi_e = \left[\xi_{\imath_1(e)}^1, \xi_{\imath_1(e)+1}^1\right) \otimes \ldots \otimes \left[\xi_{\imath_N(e)}^N, \xi_{\imath_N(e)+1}^N\right), \tag{22}$$

where $\imath_\alpha(e)$ is a map from the element indices to the indices of the knot vector Ξ^α for $\alpha = 1 \ldots N$.

Multivariate B-spline basis functions $N_i(\xi)$, with parametric coordinate $\xi = (\xi^1, \ldots, \xi^N)$, are defined through the product

$$N_i(\xi) = \prod_{\alpha=1}^N N_{\jmath_\alpha(i)}^\alpha(\xi^\alpha), \tag{23}$$

where $\jmath_\alpha(i)$ maps the global control point indices on the indices of the univariate basis functions in the direction α. Multivariate NURBS basis functions are defined by equation (20) using a weights vector $W \in \mathbb{R}^n$, where $n = \prod_{\alpha=1}^N n_\alpha$ is the number of multivariate basis functions .

Using the multivariate basis functions, an N-variate B-spline is defined by equation (19). When, in addition to a weights vector W, a set of control points $X \in \mathbb{R}^{n \times N}$ is provided, a parameterization of an N-dimensional body Ω is obtained by

$$x(\xi) = \sum_{i=1}^n R_i(\xi) X_i. \tag{24}$$

In combination with the partitioning of the multivariate parameter space by the elements Ξ_e in equation (22) this parametric map provides the definition of elements Ω_e in the physical space through equation (18).

3.3 Isogeometric finite element discretization

Let $\mathcal{S}_i^{u,h} \subset \mathcal{S}_i^u$ and $\mathcal{S}^{\bar{\eta},h} \subset \mathcal{S}^{\bar{\eta}}$ be the discrete solution spaces for the displacement field, $u(x)$, and nonlocal equivalent strain field, $\bar{\eta}(x)$, respectively. In

isogeometric analysis, these spaces are written in terms of the NURBS basis functions $R_i(\xi)$ defined in section 3.1 and 3.2 for the univariate and multivariate cases, respectively. We can approximate the displacement field and nonlocal equivalent strain field as

$$
\begin{aligned}
u_i^h(x) &= \sum_{k=1}^{n} R_k(\xi(x)) U_{ki} \\
\bar{\eta}^h(x) &= \sum_{k=1}^{n} R_k(\xi(x)) H_k
\end{aligned}
\tag{25}
$$

where $U \in \mathbb{R}^{n \times N}$ are the control point displacements, and $H \in \mathbb{R}^n$ are the control point nonlocal equivalent strains. From the displacement field, the strain, $\varepsilon(x)$, and local equivalent strain, $\eta(x)$, can be computed. In combination with the nonlocal equivalent strain field, the damage parameter, $\omega(x)$, and Cauchy stress, $\sigma(x)$, can be obtained at every point using the constitutive relations provided in section 2.1.

We use the Galerkin method to discretize the weak formulation (11) as

$$
\begin{cases}
\left(\sigma_{ij}, v_{(i,j)}^{u,h} \right)_\Omega = \left(\tilde{t}_i, v_i^{u,h} \right)_{\partial\Omega} & \forall v_i^{u,h} \in \mathcal{V}_i^{u,h} \\
\left(\bar{\eta} - \eta, v^{\bar{\eta},h} \right)_\Omega + \sum_{\beta=1}^{d/2} \left(\mathcal{H}^\beta \bar{\eta}, \mathcal{H}^\beta v^{\bar{\eta},h} \right)_\Omega = 0 & \forall v^{\bar{\eta},h} \in \mathcal{V}^{\bar{\eta},h}
\end{cases}
\tag{26}
$$

Using the NURBS basis functions, $R_i(\xi)$, as trial functions results in a system of $(N+1)n$ equations

$$
\begin{cases}
f_{\text{int},k}^{u_m} = f_{\text{ext},k}^{u_m} & \forall (k,m) \in \{1 \ldots n\} \otimes \{1 \ldots N\} \\
f_{\text{int},k}^{\bar{\eta}} = 0 & \forall k \in \{1 \ldots n\}
\end{cases}
\tag{27}
$$

which can be solved for every load step using Newton-Raphson iteration to determine the control point coefficients U_{ki} and H_k in equation (25). The internal force vectors are assembled by looping over the elements

$$
\begin{aligned}
f_{\text{int},k}^{u_m} &= \overset{n_e}{\underset{e=1}{\mathbf{A}}} f_{\text{int},k}^{e,u_m} &&= \overset{n_e}{\underset{e=1}{\mathbf{A}}} \left(\sigma_{ij}, \frac{1}{2} \left(\frac{\partial R_k}{\partial x_j} \delta_{im} + \frac{\partial R_k}{\partial x_i} \delta_{jm} \right) \right)_{\Omega_e} \\
f_{\text{int},k}^{\bar{\eta}} &= \overset{n_e}{\underset{e=1}{\mathbf{A}}} f_{\text{int},k}^{e,\bar{\eta}} &&= \overset{n_e}{\underset{e=1}{\mathbf{A}}} \left(\bar{\eta} - \eta, R_k \right)_{\Omega_e} + \sum_{\beta=1}^{d/2} \left(\mathcal{H}^\beta \bar{\eta}, \mathcal{H}^\beta R_k \right)_{\Omega_e}
\end{aligned}
\tag{28}
$$

The integrals in these expressions are evaluated on the elements Ω_e defined through equation (18). In this contribution, we use Gaussian quadrature of order $p + 1$ in each direction. Numerical integration of NURBS for analysis purposes was studied in [24] and remains an active topic of research. In order to evaluate the integrals, the Jacobian of the isogeometric map needs to be evaluated at every integration point. Since rational basis functions are used,
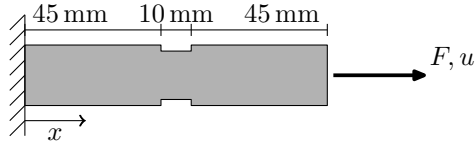
Figure 3: Schematic representation of a one-dimensional rod loaded in tension. The cross-sectional area of the rod is $10\,\text{mm}^2$ except for the central section where it is equal to $9\,\text{mm}^2$.

this requires application of the quotient rule. Since higher-order derivatives with respect to the physical coordinate x are used in this contribution, higher-order derivatives of the parametric map are also required. These higher-order derivatives are obtained by application of the chain rule to the differentiation of the NURBS basis functions with respect to the physical coordinates [12].

The consistent tangent matrix, required by the Newton-Raphson procedure, can be obtained by differentiation of (28) with respect to the control point variables in equation (25). Evaluation of the tangent requires the derivatives of the stress, σ, with respect to the strain, ε, and nonlocal equivalent strain, $\bar{\eta}$. These derivatives are provided through the constitutive behavior elaborated in section 2.1. The derivative of the local equivalent strain, η, with respect to the strain tensor follows from the equivalent strain law, $\eta = \eta(\varepsilon)$.

4   NUMERICAL SIMULATIONS

4.1   One-dimensional rod loaded in tension

We consider a one-dimensional rod loaded in tension as shown in Figure 3. The $10\,\text{mm}$ wide central section of the rod has a reduced cross-sectional area in order to develop a centralized damage zone. The modulus of elasticity of the rod is $E = 20\,\text{GPa}$, and the Cauchy stress is written as $\sigma = (1 - \omega)E\varepsilon$. As a damage law we consider [7]

$$\omega(\kappa) = \begin{cases} 0 & \kappa \leq \kappa_0 \\ \frac{\kappa_u}{\kappa} \frac{\kappa - \kappa_0}{\kappa_u - \kappa_0} & \kappa > \kappa_0 \end{cases} \tag{29}$$

with $\kappa_0 = 1 \cdot 10^{-4}$ and $\kappa_u = 0.0125$. We define the local equivalent strain law as $\eta = \langle \varepsilon \rangle$ where $\langle \cdot \rangle$ is the Macaulay bracket and take the nonlocal length scale in (5) equal to $l_c = \sqrt{2}\,\text{mm}$.

Force-displacement curves have been determined for the second-, fourth- and sixth-order implicit gradient models and for the nonlocal damage formulation. A dissipation-based path-following constraint [25] is used to trace the equilibrium path beyond the snapback point. Mesh convergence studies have been performed using uniform meshes with 80, 160, 320, 640 and 1280 elements of orders 1, 2 and 3. The control points are equidistantly spaced and all control weights are equal to 1, which leads to a linear parameterization of the domain. An overview

of the meshes is given in Table 1. Note that in contrast to higher-order finite elements, the number of degrees of freedom is practically independent of the order of the basis (since for practical meshes $p \ll n_e$).

The force-displacement results for the second-order gradient formulation obtained on all meshes are presented in Figure 4. Increasing the order of the basis from linear to quadratic significantly improves the rate of convergence. A further increase of the order of the basis to cubics has minor effects on the mesh convergence behavior. This is explained by the fact that both quadratic and cubic basis functions are unable to accurately represent the solution in the region where loss of ellipticity has occured. Accurate results for the second-order formulation are obtained using 1280 elements of any order. Force-displacement results for the fourth-order gradient formulation are shown in Figure 5. The presence of fourth-order spatial derivatives in this formulation requires C^1-continuity. For that reason, meaningful results are only obtained on quadratic and cubic meshes. The response obtained on the 1280 element meshes cannot be visually distinguished from that obtained on the 640 element meshes. A very accurate result is already obtained on the 320 element mesh. The improved convergence behavior of the fourth-order formulation compared to the second-order formulation is attributed to the fact that smoother results are obtained. The increased smoothness of the fourth-order formulations compared to the second-order formulation is closely related to the postponed loss of ellipticity for these formulations as demonstrated by the dispersion analysis performed in [9]. Meaningful results for the sixth-order formulation are only obtained on cubic meshes, and are shown in Figure 6. The convergence behavior of the sixth-order formulation closely resembles that of the fourth-order formulation. In Figure 7 we present the results obtained on all meshes for the nonlocal formulation. Compared to the results obtained using the second-order formulation, the nonlocal formulation shows superior convergence behavior for the linear, quadratic and cubic meshes. As expected, the difference in convergence behavior diminishes as the order of the gradient formulation is increased. In fact, the results for the nonlocal formulation obtained using cubic basis functions can hardly be distinguised from those obtained using the sixth-order formulation (Figure 6). For the purpose of comparing the various formulations, the accuracy of the solutions obtained on the 1280 cubic element meshes suffices. A detailed study of the convergence rates is a topic of future research.

In Figure 8 we show a comparison of the various formulations. All results are obtained on a mesh with 1280 cubic elements. The results are in excellent agreement with those reported in e.g. [7] and [9]. As in [9] it is observed that the incorporation of fourth-order derivatives in the implicit scheme improves the results, in the sense that the obtained force-displacement curve is closer to that of the nonlocal formulation. Consistent with this observation we find that the sixth-order formulation gives an even better approximation of the nonlocal result. Similar trends are observed from the final damage profiles (see Figure 8). The sixth-order formulation is found to be very efficient since the results are in good agreement with the nonlocal formulation, while the involved computational effort is very small compared to the nonlocal formulation. Based on the

Linear B-spline ($p = 1$)					
Number of elements, n_e	80	160	320	640	1280
Number of basis functions, n	81	161	321	641	1281

Quadratic B-spline ($p = 2$)					
Number of elements, n_e	80	160	320	640	1280
Number of basis functions, n	82	162	322	642	1282

Cubic B-spline ($p = 3$)					
Number of elements, n_e	80	160	320	640	1280
Number of basis functions, n	83	163	323	643	1283

Table 1: Meshes used for the uniaxial rod simulation. Note that for this case $n = n_e + p$.
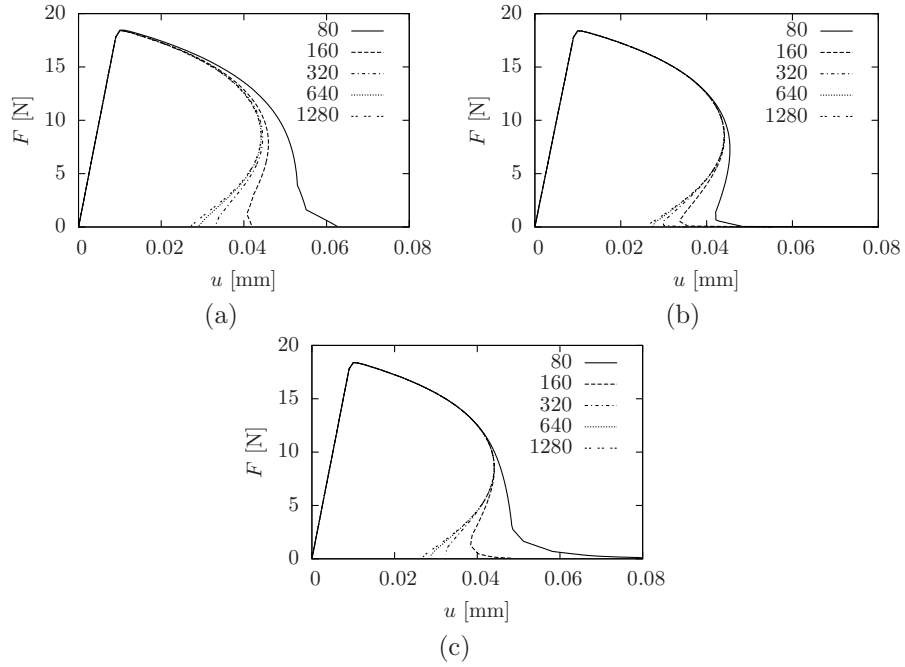
Figure 4: Mesh convergence studies for the rod using the second-order gradient formulation, discretized using linear B-splines (a), quadratic B-splines (b), and cubic B-splines (c). The key labels indicate the number of elements.
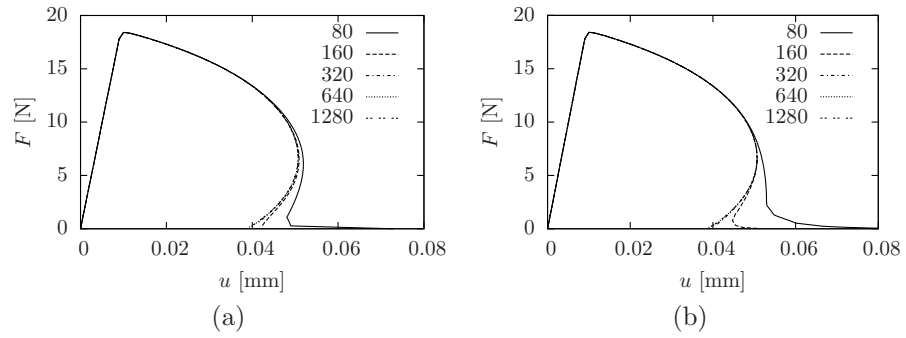
Figure 5: Mesh convergence studies for the rod using the fourth-order gradient formulation, discretized using quadratic B-splines (a), and cubic B-splines (b). The key labels indicate the number of elements.
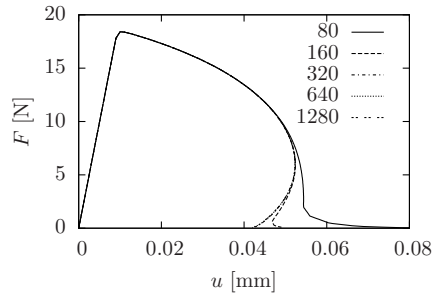
Figure 6: Mesh convergence studies for the rod using the sixth-order gradient formulation, discretized using cubic B-splines. The key labels indicate the number of elements.
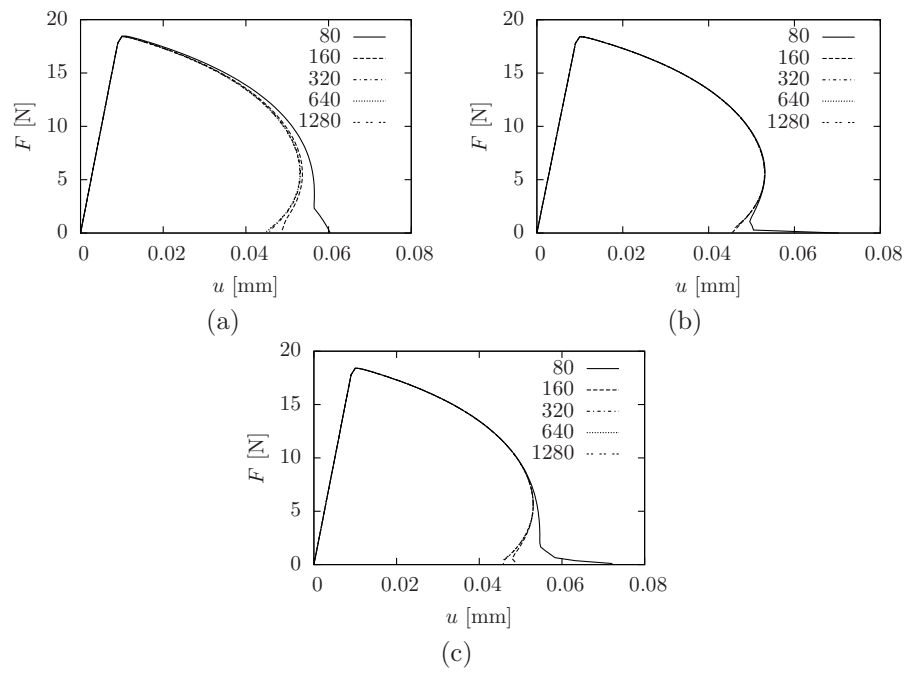
Figure 7: Mesh convergence studies for the rod using the nonlocal formulation, discretized using linear B-splines (a), quadratic B-splines (b), and cubic B-splines (c). The key labels indicate the number of elements.

14
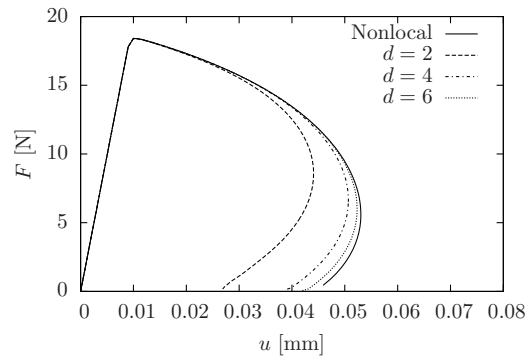
Figure 8: Force-displacement diagrams for the rod loaded in tension using the nonlocal formulation and d-th order gradient formulations. All results are obtained using 1280 cubic elements.
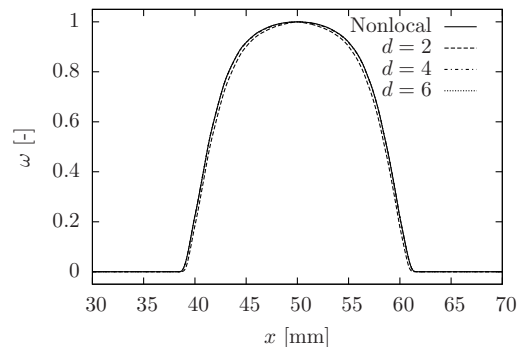
Figure 9: Final damage profile for the rod loaded in tension using the nonlocal formulation and the d-th order gradient formulations. All results are obtained using 1280 cubic elements.

resemblance of the sixth-order and nonlocal result it is concluded that, for the considered simulation, ignoring the nonlocal equivalent strain boundary terms appearing in the gradient formulation has a minor effect on the results.

4.2 Three-point bending beam

As a second numerical experiment we consider the three-point bending beam experiment considered in [9] and shown in Figure 10. The $1000 \times 300\,\text{mm}^2$ beam is supported by hinges on the left and right bottom corners, and is loaded by a distributed load $\bar{t}$ over the central $100\,\text{mm}$ section of the specimen.

A linear isotropic material is considered with modulus of elasticity $E = 20\,\text{GPa}$ in the undamaged state and Poisson's ratio $\nu = 0.2$. Plane strain con-
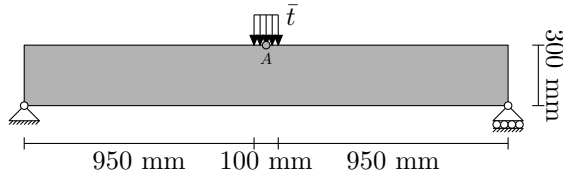
Figure 10: Three-point bending specimen. The thickness of the specimen is 50 mm.

ditions are assumed, and the local equivalent strain is given by

$$\eta(\varepsilon) = \sqrt{\langle \varepsilon_i \rangle^2} = \sqrt{\langle \varepsilon_1 \rangle^2 + \langle \varepsilon_2 \rangle^2} \qquad (30)$$

where ε_1 and ε_2 are the principal strains of the two-dimensional strain tensor. The Macaulay bracket distinguishes the cases of tension and compression. The following damage law as proposed in [26] is used

$$\omega(\kappa) = \begin{cases} 0 & \kappa \leq \kappa_0 \\ 1 - \frac{\kappa_0}{\kappa} \left\{ (1 - \alpha) + \alpha \exp\left[\beta(\kappa_0 - \kappa)\right] \right\} & \kappa > \kappa_0 \end{cases} \qquad (31)$$

with parameters $\kappa_0 = 1 \cdot 10^{-4}$, $\alpha = 0.99$ and $\beta = 500$. The nonlocal length scale is taken as $l_c = 20$ mm.

Force-displacement curves are obtained using the meshes shown in Figure 11 with linear, quadratic and cubic basis functions. A summary of the mesh parameters is given in Table 2. Note that in two dimensions the number of basis functions is also practically independent of the order of the formulation, in contrast to traditional cubic finite elements. The control point weights are all taken equal to 1, and control points are placed such that a bilinear parameterization of the beam is obtained. The force F is defined as the distributed load $\bar{t}$ times the width to which it is applied. The displacement u is measured by the downward displacement of point A, as indicated in Figure 10. This displacement is used as a path-following constraint to trace the equilibrium path.

In Figure 12 we show the response curves for the second-order gradient formulation obtained on all meshes. As in the one-dimensional study in section 4.1 we see a significant improvement in the convergence rate when using quadratic basis functions instead of linear basis functions. Accurate results are obtained using Mesh 4 with quadratic or cubic basis functions. The results obtained on the quadratic and cubic meshes for the fourth-order formulation are shown in Figure ??. For both the quadratic and cubic basis functions, the results obtained on Mesh 4 cannot be visually distinguished from those obtained on Mesh 3. The same holds for the results obtained for the sixth-order formulation, as shown in Figure 14. Due to the considerable computational effort required, the mesh convergence behavior of the nonlocal formulation is only studied using Mesh 1, 2 and 3. As seen from Figure 15, a significant change in the force-displacement curves is observed when comparing the Mesh 2 and Mesh 3 results

16
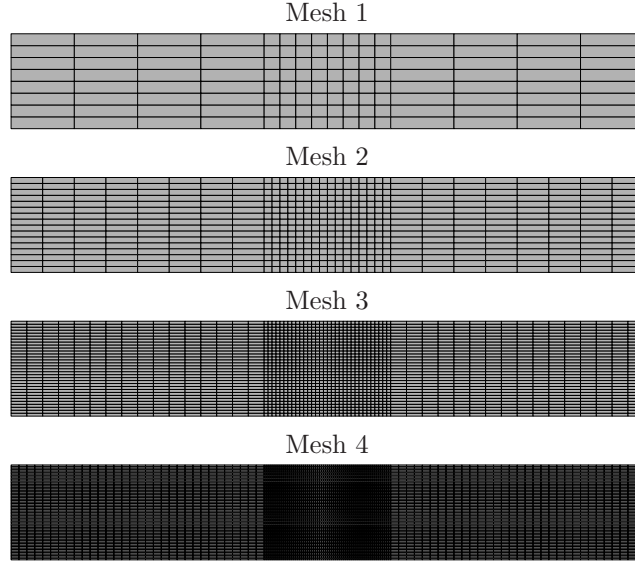
Figure 11: Meshes for the three-point bending specimen.

Linear B-spline ($p = 1$)

	Mesh 1	Mesh 2	Mesh 3	Mesh 4
Number of elements, n_e	128	512	2048	8192
Number of basis functions, n	153	561	2145	8385

Quadratic B-spline ($p = 2$)

	Mesh 1	Mesh 2	Mesh 3	Mesh 4
Number of elements, n_e	128	512	2048	8192
Number of basis functions, n	180	612	2244	8580

Cubic B-spline ($p = 3$)

	Mesh 1	Mesh 2	Mesh 3	Mesh 4
Number of elements, n_e	128	512	2048	8192
Number of basis functions, n	209	665	2345	8777

Table 2: Meshes used for the three-point bending beam. Note that for these meshes $n = (\sqrt{2n_e} + p)(\sqrt{n_e/2} + p)$.
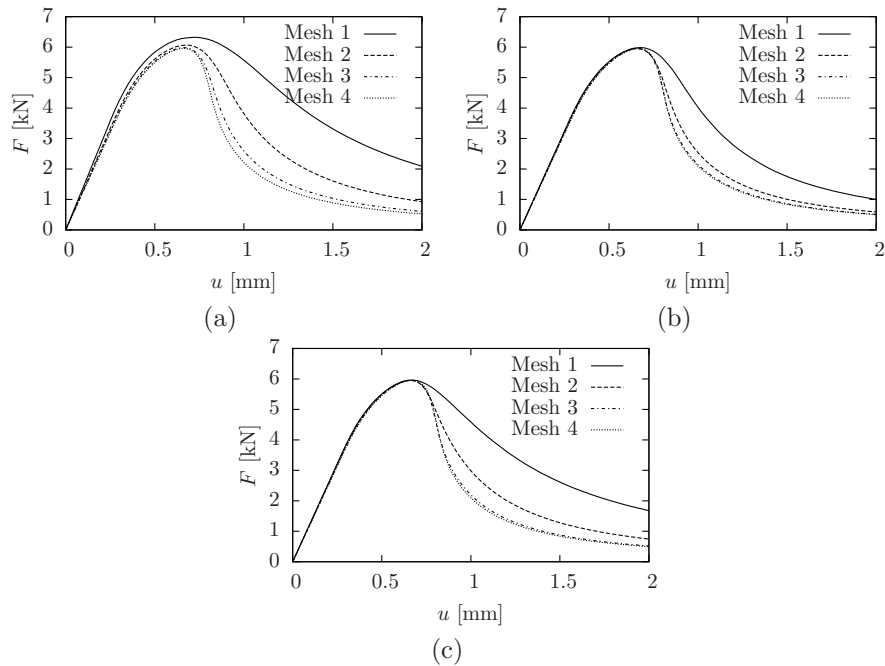
Figure 12: Mesh convergence studies for the three-point bending beam using the second-order gradient formulation, discretized using linear B-splines (a), quadratic B-splines (b), and cubic B-splines (c) .

with linear basis functions. When using quadratic basis function, the response curves cannot be visually distinguised. For the purpose of comparing the various formulations, the result of the nonlocal formulation obtained on the quadratic Mesh 3 is sufficiently accurate.

In Figure 16 the results of the various formulations are compared. Typical damage profiles are shown in Figure 17. Upon increasing the order of the formulation the approximation of the nonlocal result is improved. Increasing the order of the formulation increases the total amount of dissipated energy. This is caused by the additional smoothing effect of the higher-order derivatives. For the considered problem, the sixth-order formulation is observed to be very efficient, since it accurately approximates the nonlocal result, whereas the involved computational effort is negligible compared to the nonlocal formulation. As in the case of the rod simulation, setting all the Neumann boundary conditions (10) for the equivalent strain field to zero does not have a significant effect on the results.

18
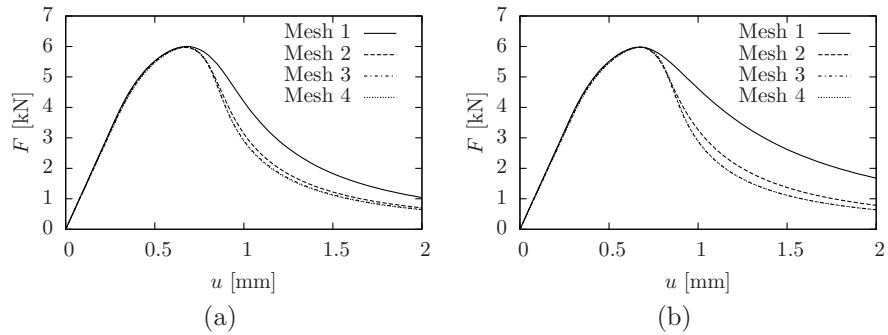
Figure 13: Mesh convergence studies for the three-point bending beam using the fourth-order gradient formulation, discretized using quadratic B-splines (a), and cubic B-splines (b).

labelfig:threepointconvergence4th
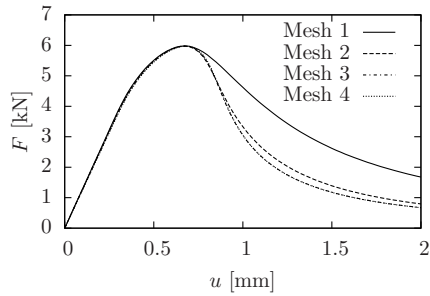
Figure 14: Mesh convergence studies for the three-point bending beam using the sixth-order gradient formulation, discretized using cubic B-splines.
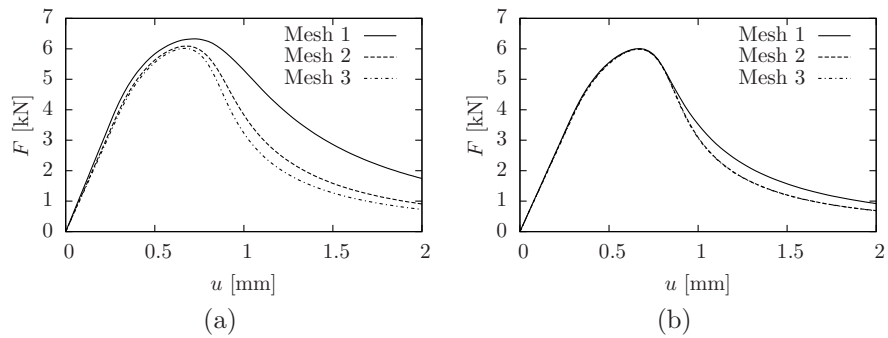

Figure 15: Mesh convergence studies for the three-point bending beam using the nonlocal formulation, discretized using linear B-splines (a), and quadratic B-splines (b).
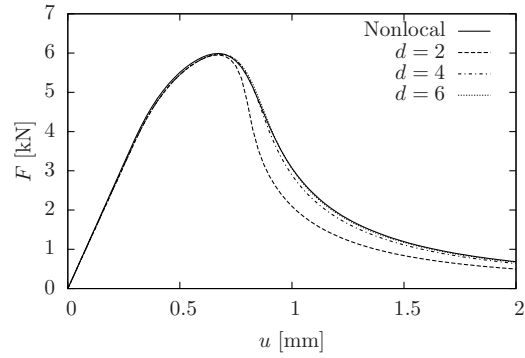
Figure 16: Force-displacement results for the three-point bending beam speci-men using the nonlocal formulation and d-th order gradient formulations. All results for the gradient formulation are obtained using Mesh 4 with cubic basis functions. The result for the nonlocal formulation is obtained on Mesh 3 with quadratic basis functions.

$$u = 0.875\,\text{mm}$$

$$u = 2.00\,\text{mm}$$
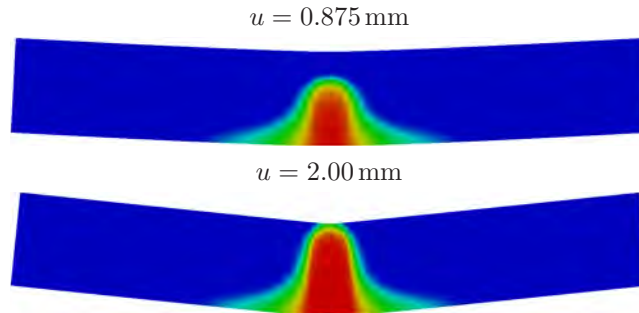
Figure 17: Damage profiles for the three-point bending experiment obtained using the fourth-order gradient formulation. Undamaged material is indicated in blue, fully damaged material in red. Deformations are 50 times amplified.

5 CONCLUSIONS

Isogeometric analysis allows for the construction of smooth basis functions on complex domains, providing an appropriate solution space for higher-order differential equations. Dirichlet boundary conditions can be applied by specifying control variables along the boundary, in the same way as nodal variables are specified for traditional finite elements.

Isogeometric analysis is shown to be a very good candidate for the discretization of higher-order gradient damage formulations. Using cubic basis functions allows for the discretization of the sixth-order gradient damage formulation. Since, from a practical point of view, the number of degrees of freedom is independent of the polynomial order of the basis functions, the fourth- and sixth-order formulation require only slightly more computational effort than the second-order formulation. This makes it practical to study the convergence of the implicit gradient damage formulation toward the nonlocal formulation upon increasing its order.

Numerical simulations have been performed for a one-dimensional rod loaded in tension, for which a univariate B-spline basis is constructed. A two-dimensional three-point bending beam specimen is discretized using a bivariate NURBS patch. For both simulations it is observed that the result of the nonlocal formulation is approached upon increasing the order of the gradient damage formulation. Since the computational effort involved in the nonlocal formulation is much larger than that for the gradient approximations, increasing the order of the gradient formulation yields efficient approximations of the nonlocal result. For the two simulations considered, the sixth-order formulation gave an accurate approximation.

References

[1] J. Lemaitre and J. L. Chaboche. *Mechanics of solid materials*. Cambridge University Press, Cambridge, 1990.

[2] J. H. P. de Vree, W. A. M. Brekelmans, and M. A. J. van Gils. Comparison of nonlocal approaches in continuum damage mechanics. *Computers & Structures*, 55(4):581–588, 1995.

[3] R. de Borst. *Encyclopedia of Computational Mechanics*, volume 2: Solids and Structures, chapter 10: Damage, material instabilities, and failure, pages 335–373. Wiley, Chichester, 2004.

[4] K. J. Willam, N. Bicanic, and S. Stura. Constitutive and computational aspects of strain-softening and localization in solids. In *Constitutive equations: macro and computational aspects*, page 233. ASME, 1984.

[5] W. A. M. Brekelmans and J. H. P. de Vree. Reduction of mesh sensitivity in continuum damage mechanics. *Acta Mechanica*, 110(1):49–56, 1995.

[6] G. Pijaudier-Cabot and Z. P. Bažant. Nonlocal damage theory. *Journal of Engineering Mechanics*, 113(10):1512–1533, 1987.

[7] R. H. J. Peerlings, R. de Borst, W. A. M. Brekelmans, and J. H. P. de Vree. Gradient enhanced damage for quasi-brittle materials. *International Journal for Numerical Methods in Engineering*, 39(19):3391–3403, 1996.

[8] A. Huerta and G. Pijaudier-Cabot. Discretization influence on regularization by two localization limiters. *Journal of Engineering Mechanics*, 120(6):1198–1218, 1994.

[9] H. Askes, J. Pamin, and R. de Borst. Dispersion analysis and element-free Galerkin solutions of second- and fourth-order gradient-enhanced damage models. *International Journal for Numerical Methods in Engineering*, 49(6):811–832, 2000.

[10] H. Sakurai. Element-free methods vs. mesh-less CAE. *International Journal of Computational Methods*, 3(4):445–464, 2006.

[11] T. J. R. Hughes, J. A. Cottrell, and Y. Bazilevs. Isogeometric analysis: CAD, finite elements, NURBS, exact geometry and mesh refinement. *Computer Methods in Applied Mechanics and Engineering*, 194(39–41):4135–4195, 2005.

[12] J. A. Cottrell, T. J. R. Hughes, and Y. Bazilevs. *Isogeometric Analysis: Toward Integration of CAD and FEA*. Wiley, Chichester, 2009.

[13] H. Gómez, V. M. Calo, Y. Bazilevs, and T. J. R. Hughes. Isogeometric analysis of the Cahn-Hilliard phase-field model. *Computer Methods in Applied Mechanics and Engineering*, 197(49-50):4333–4352, 2008.

[14] D. J. Benson, Y. Bazilevs, E. De Luycker, M. C. Hsu, M. A. Scott, T. J. R. Hughes, and T. Belytschko. A generalized finite element formulation for arbitrary basis functions: from isogeometric analysis to XFEM. *International Journal for Numerical Methods in Engineering*, DOI: 10.1002/nme.2864, 2010.

[15] L. J. Sluys and R. de Borst. Dispersive properties of gradient-dependent and rate-dependent media. *Mechanics of Materials*, 18(2):131–149, 1994.

[16] D. F. Rogers. *An Introduction to NURBS*. Academic Press, San Diego, 2001.

[17] T. W. Sederberg, J. Zheng, A. Bakenov, and A. Nasri. T-splines and T-NURCCs. *ACM Transactions on Graphics*, 22(3):477–484, 2003.

[18] M. J. Borden, M. A. Scott, J. A. Evans, and T. J. R. Hughes. Isogeometric finite element data structures based on Bézier extraction. *International Journal for Numerical Methods in Engineering*, 2010.

[19] M. G. Cox. The numerical evaluation of B-splines. *IMA Journal of Applied Mathematics*, 10(2), 1972.

[20] C. de Boor. On calculating with B-splines. *Journal of Approximation Theory*, 6(1):50–62, 1972.

[21] L. Piegl and W. Tiller. *The NURBS Book*. Springer-Verlag, Berlin, second edition, 1997.

[22] G. Farin. *Curves and Surfaces for CAGD*. Academic Press, Inc., 1993.

[23] J. A. Cottrell, T. J. R. Hughes, and A. Reali. Studies of refinement and continuity in isogeometric structural analysis. *Computer Methods in Applied Mechanics and Engineering*, 196(41–44):4160–4183, 2007.

[24] T. J. R. Hughes, A. Reali, and G. Sangalli. Efficient quadrature for NURBS-based isogeometric analysis. *Computer Methods in Applied Mechanics and Engineering*, 199(5-8):301–313, 2010.

[25] C. V. Verhoosel, J. J. C Remmers, and M. A. Gutiérrez. A dissipation-based arc-length method for robust simulation of brittle and ductile failure. *International Journal for Numerical Methods in Engineering*, 77(9):1290–1321, 2009.

[26] M. G. D. Geers, R. de Borst, W. A. M. Brekelmans, and R. H. J. Peerlings. Strain-based transient-gradient damage model for failure analyses. *Computer Methods in Applied Mechanics and Engineering*, 160(1-2):133–153, 1998.